Electronic Supplementary Material (ESI) for Materials Chemistry Frontiers.
This journal is © the Partner Organisations 2024

Interfacial modification engineering for efficient and stable MA-free wide-bandgap perovskite solar cells by grain regrowth

Hao Huang[1], Ziyu Li[1], Zhijia Chen, Denggao Li, Hongxi Shi, Keqi Zhu, Chenyu Wang, Zhangbo Lu, Shihua Huang, Dan Chi*

Provincial Key Laboratory of Solid-State Optoelectronic Devices Zhejiang Normal University, Jinhua 321004, China

E-mail: chidan@zjnu.edu.cn

[1] Hao Huang and Ziyu Li contributed equally to this work.

Keywords: MA-free wide-bandgap perovskite, grain regrowth, interfacial modification, defect passivation, high stability

Materials

Nickel oxide nanoparticles (NiO_x) and cesium iodide (CsI, 99.99% purity) were purchased from Advanced Election Technology Co., Ltd. Me-4PACz ($C_{18}H_{22}NO_3P$, >99.0% purity), lead(II) iodide (PbI_2, >99.99% purity), lead(II) bromide ($PbBr_2$, >99.99% purity), formamidinium iodide ($HC(NH_2)_2I$, FAI, ≥99.5% purity), lead(II) chloride ($PbCl_2$, >99.99% purity), and GuSCN were purchased from Xi'an Yuri Solar Co., Ltd. Absolute alcohol was obtained from Sinopharm Chemical Reagent Co., Ltd. Tin dioxide (SnO_2) was purchased from Dongguan Nanofrontier Microelectronic Equipment Co., Ltd. Dimethyl sulfoxide (DMSO, 99.9%), N,N-dimethylformamide (DMF, 99.9%), and isopropyl alcohol (IPA, ≥99.7% purity) were purchased from Sigma-Aldrich. All materials were commercially sourced and utilized as received.

Solution Preparation

NiO_x NPs were dispersed in deionized water at a concentration of 30 mg/mL using ultrasonic treatment for approximately 2 hours. Me-4PACz was dissolved in absolute alcohol at a concentration of 1 mg/mL. The perovskite solution (1.3 M) was prepared by dissolving FAI, PbI_2, $PbBr_2$, and CsI in a DMF: DMSO mixed solvent (5:1 volume ratio) with a stoichiometric ratio of $Cs_{0.2}FA_{0.8}Pb(I_{0.8}Br_{0.2})_3$. Subsequently, 1.5 mol% of $PbCl_2$ was added to the perovskite solution, and the mixture was stirred at 60 °C for 2 hours. GuSCN was dissolved in isopropyl alcohol (IPA) to form solutions with concentrations of 15 mM, 25 mM, and 35 mM, respectively.

Device fabrication

ITO conductive glass was cleaned sequentially with glass cleaner, deionized water, and isopropyl alcohol under ultrasonic treatment for 15 minutes, respectively, followed by drying with nitrogen gas. Subsequently, the substrates were treated in a UV-ozone cleaner for 30 minutes. A hole

transport layer (HTL) was formed by spin-coating a NiO_x nanoparticle solution onto the ITO glass at 2000 rpm for 30 seconds and annealing in air at 150 °C for 30 minutes. Solutions of Me-4PACz and GuSCN were prepared in a glovebox. A Me-4PACz precursor solution in absolute alcohol (1 mg/mL) was then spin-coated onto the NiO_x substrates at 6000 rpm for 30 seconds, followed by annealing at 100 °C for 10 minutes. A two-step spin-coating process was used to deposit the perovskite film. First, the substrate was covered with the perovskite precursor solution and rotated at 1000 rpm for 15 seconds, followed by a spin-coating step at 6000 rpm for 60 seconds. During the second step, approximately 150 μL of chlorobenzene was dropped onto the center of the spinning substrate 30 seconds before the end of the program. Immediately after spin-coating, the substrates were placed on a hotplate and annealed for 10 minutes at 100 °C. After annealing at 100 °C for 10 minutes, the perovskite active layer was modified with GuSCN and subsequently annealed again at 100 °C for 10 minutes. Finally, C60 was deposited by thermal evaporation, followed by atomic layer deposition (ALD) of SnO_2 for 30 minutes in the air. The perovskite solar cell (PSC) fabrication was completed by thermal evaporation of the Ag electrode. The effective area of the PSC was determined using an aperture shield with an area of 0.0588 cm^2. To prepare transparent electrode PSCs, C60 was first deposited on the perovskite layer by thermal evaporation, followed by atomic layer deposition of SnO_2. ITO layers with a thickness of 400 nm were deposited by magnetron sputtering under the following conditions: 30 W for 10 minutes and 60 W for 20 minutes. Finally, a finger-like Ag electrode was prepared by thermal evaporation to complete the transparent electrode PSCs.

Characterization

The surface and cross-sectional morphology of the perovskite active layer were analyzed using field emission scanning electron microscopy (SEM) with a Merlin microscope from Zeiss. The

surface elemental distributions of perovskites without and with GuSCN modification were measured by X-ray photoelectron spectroscopy (XPS) using an Escalab 250Xi instrument from Thermo Fisher Scientific. Current density-voltage (J-V) curves for all devices were obtained with a solar simulator (Sol3A from Newport) and a digital sourcemeter (2400 from Keithley). Space-charge limited current (SCLC) measurements were performed to evaluate the defect density of control and target devices, providing further insight into the defect passivation effect. The crystallinity of the perovskite active layer was investigated using X-ray diffraction (XRD) with a MiniFlex600 diffractometer from Rigaku. The absorbance spectra of the perovskite films were measured using a Lambda 365 UV-Vis spectrophotometer from PerkinElmer. The contact angles of the perovskite films and NiO_x were determined using a contact angle test apparatus (SL200KS from American Kono Group). The TRPL spectra (with excitation at 430 nm and emission at 740 nm) were characterized by full-function fluorescence phosphorescence spectroscopy (FLS920, Edinburgh Instruments, EI) with an IRF of ≈0.4 ns.

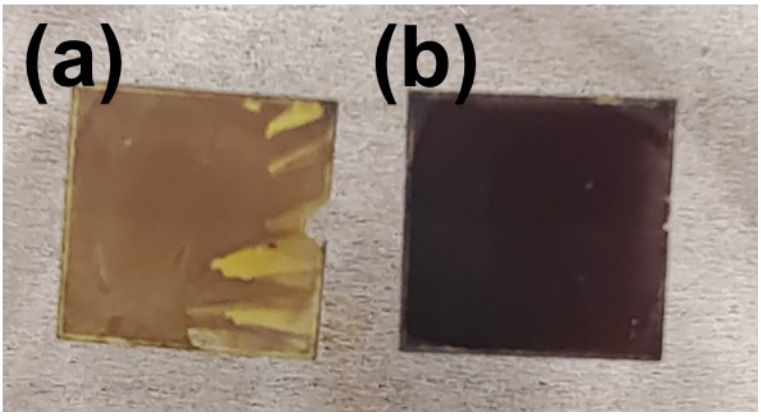

Fig. S1 (a) Perovskite with the post-treatment and without thermal annealing, (b) Perovskite with the post-treatment and thermal annealing.

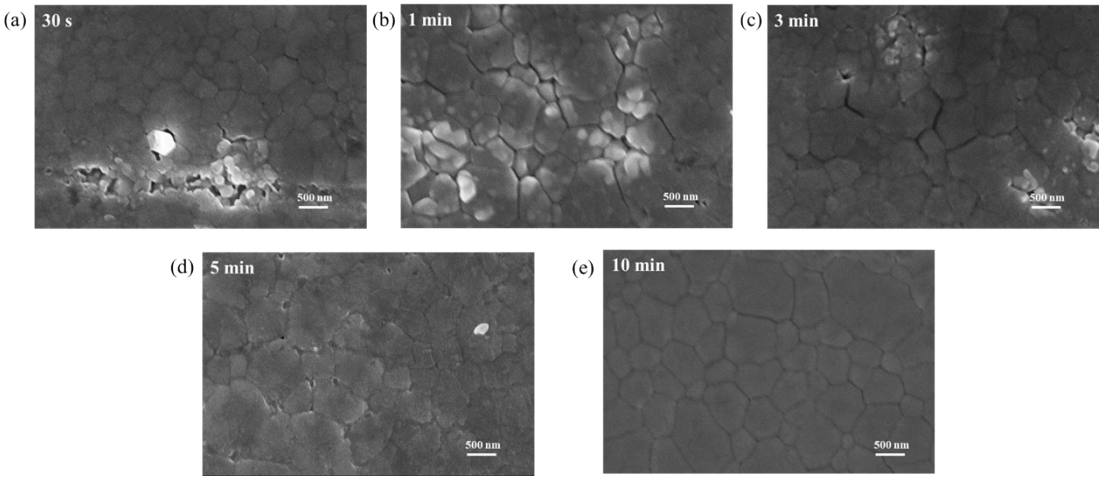

Fig. S2 SEM images of perovskite layers treated with GuSCN and thermal annealed with different times (a) 0.5 min, (b) 1 min, (c) 3 min, (d) 5 min, and (e) 10 min.

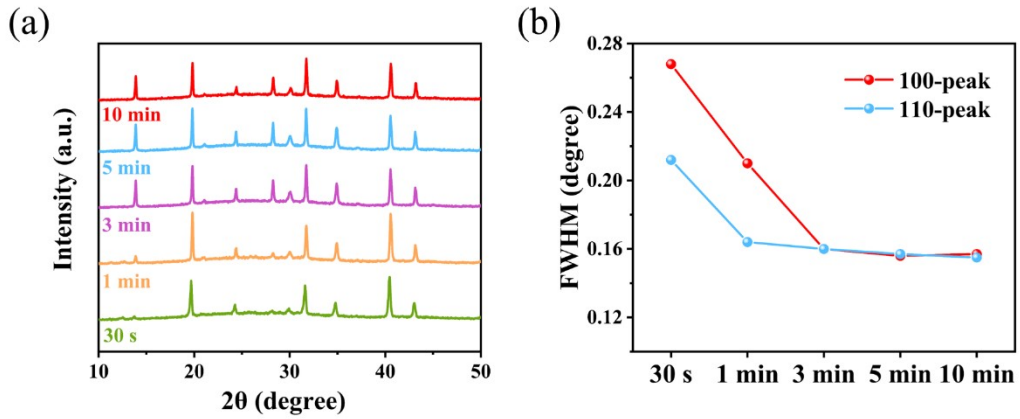

Fig. S3 (a) XRD patterns and (b) the 100-peak half-peak width and the 110-peak half-peak width of perovskite thin films prepared with GuSCN and thermal-annealed at different times.

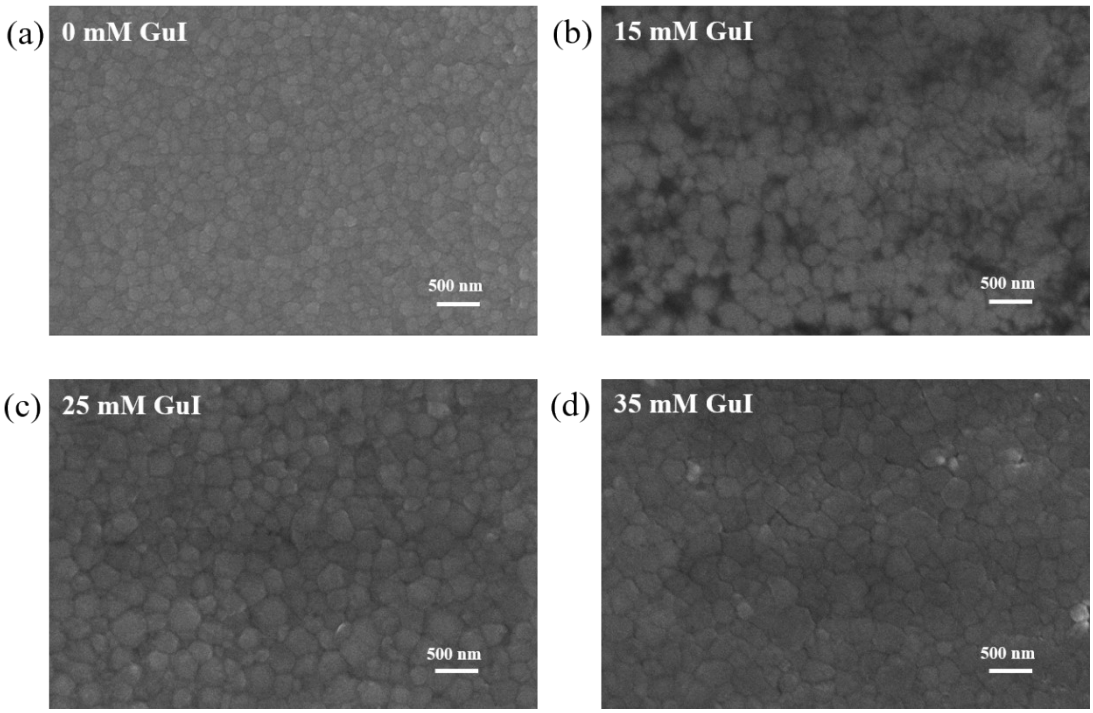

Fig. S4 SEM images of perovskite layers treated with different concentrations of GuI (a) 0 mM, (b) 15 mM, (c) 25 mM, and (d) 35 mM.

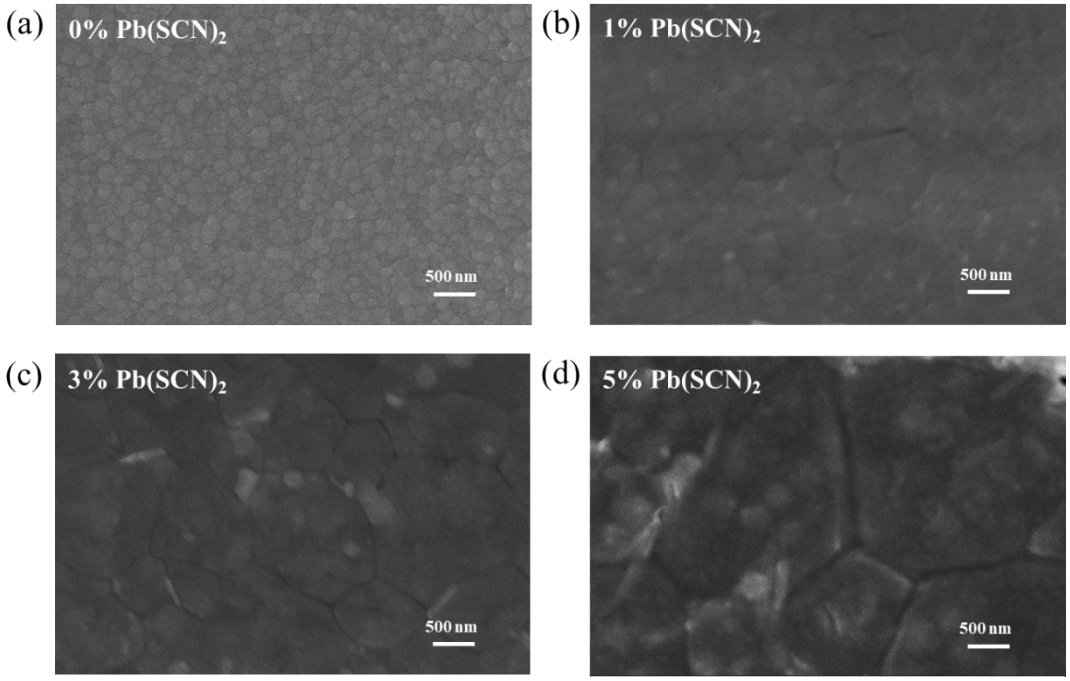

Fig. S5 SEM images of perovskite layers with different concentrations of $Pb(SCN)_2$ additive (a) 0 mol%, (b) 1 mol%, (c) 3 mol%, and (d) 5 mol%.

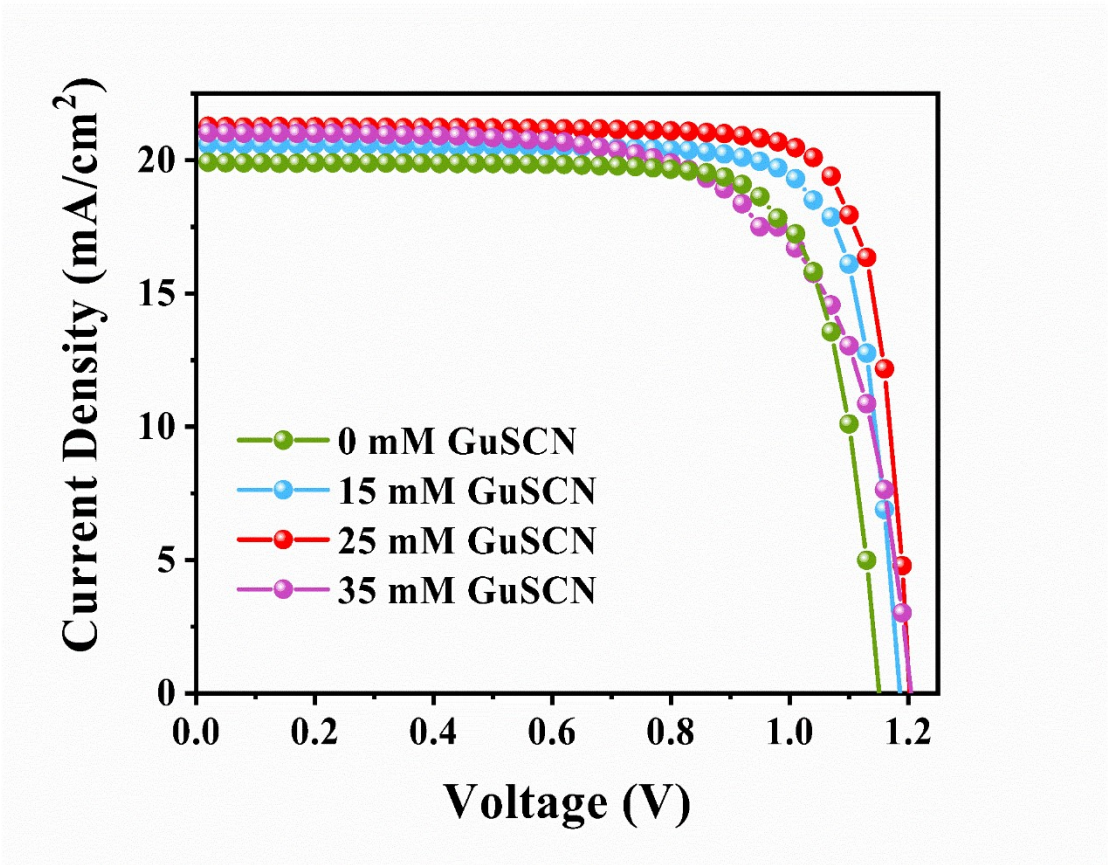

Fig. S6 The current density-voltage (JV) curves of PSCs post-treated with different concentrations of GuSCN.

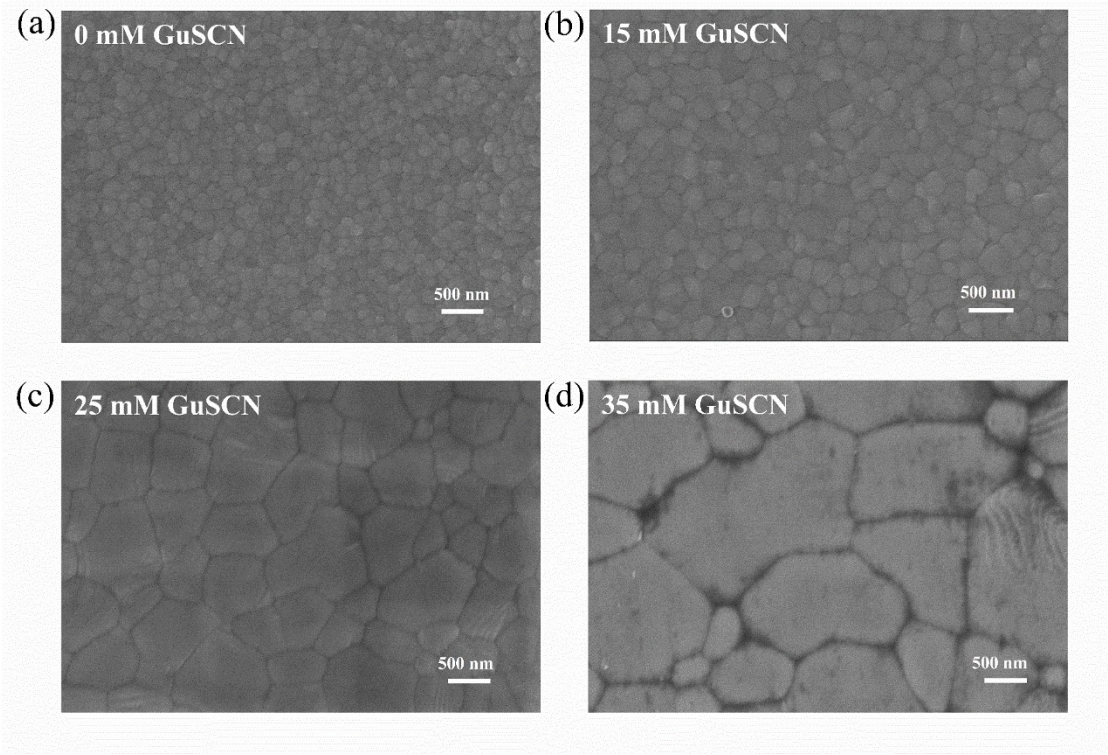

Fig. S7 SEM images of perovskite films treated with different concentrations of GuSCN and then deposited with C60/SnO_2.

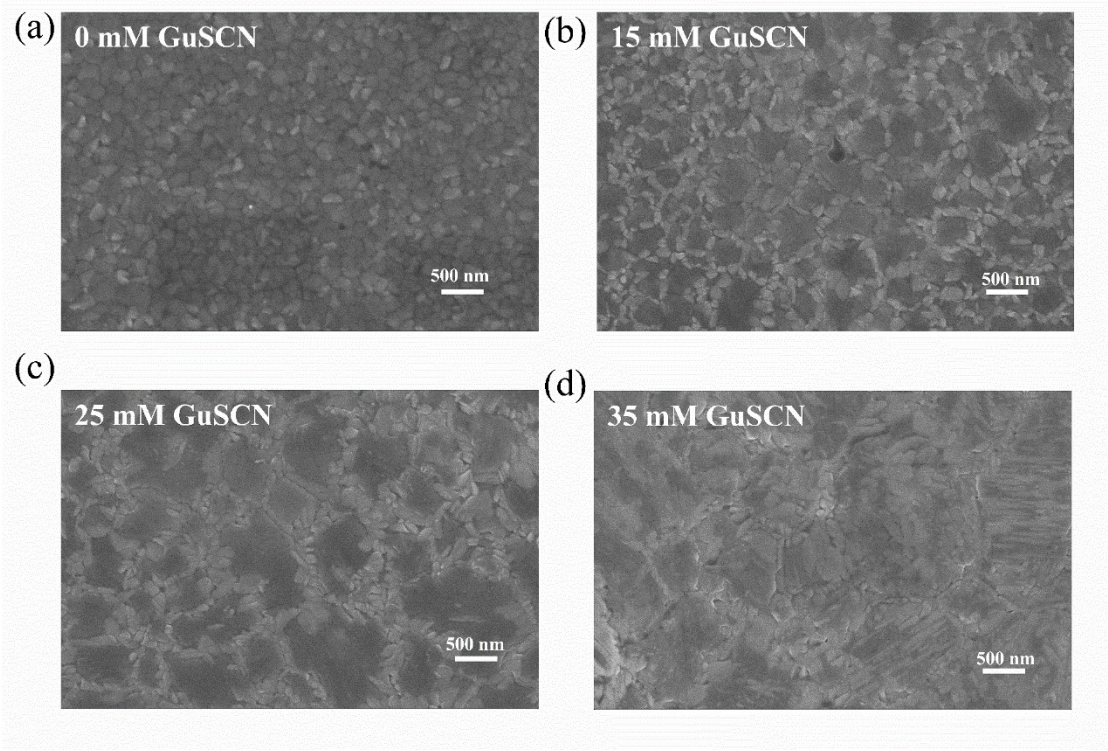

Fig. S8 SEM images of perovskite films treated with different concentrations of GuSCN and then put into an ALD machine and heated at 100 ℃ for 30 minutes.

We have measured the dark JV curves of the target (with GuSCN) and control (without GuSCN) devices. The ideality factor and reverse saturation current density were calculated by using the basic equation:

$$j = j_0\left(e^{qV/nk_BT} - 1\right). \quad (1)$$

Where k_B, T, n and j_0 represent Boltzmann constant, temperature, ideality factor and reverse saturation current density, respectively. As the value of e^{qV/nk_BT} is much larger than 1, we can simplify the basic equation to equation 2:

$$j = j_0\left(e^{qV/nk_BT}\right) \quad (2)$$

Then taking the natural logarithm of both sides of the equation gives the following equation:

$$ln(j) = ln(j_0) + \left(\frac{q}{nk_BT}\right)V \quad (3)$$

q/k_BT=38.46

Finally, the slope gives q/nk_BT and the intercept gives ln (j_0).

The n and j_0 of the target device are 1.78 and 1.59 x 10^{-10} mA/cm^2 which are much lower than the 2.00 and 4.49 x 10^{-9} mA/cm^2 of the control device, as exhibited in Fig. S9. We characterized the dark current curves of the devices, but limitations in the test software (Oriel IV Test Station. vi) prevented us from capturing currents below 10^{-8} A. These low-current values are insignificant for our analysis since only data points with V > 0.5 V will be used to fit Eq. (3) and calculate the n and j_0.

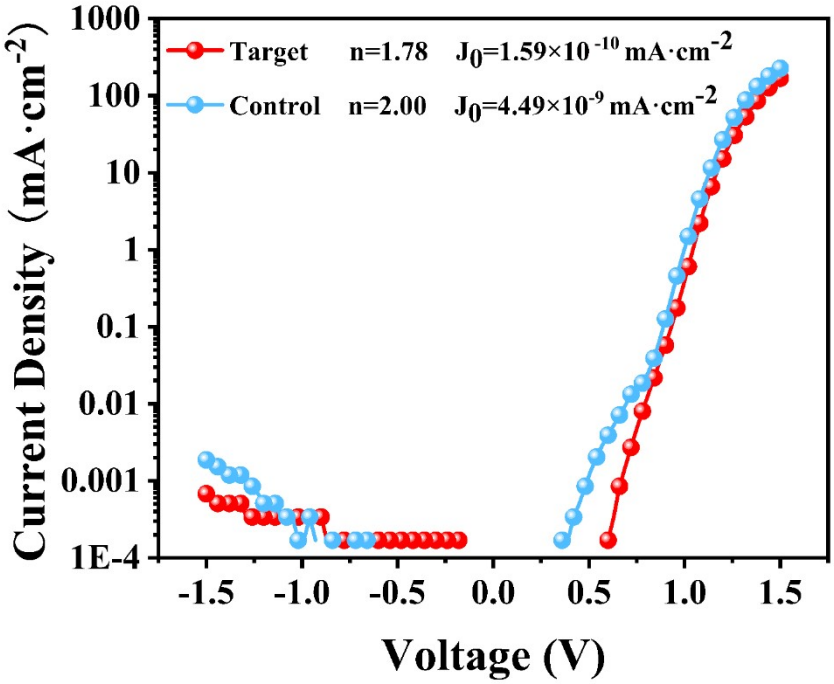

Fig. S9 Dark current to voltage curves of target and control devices.

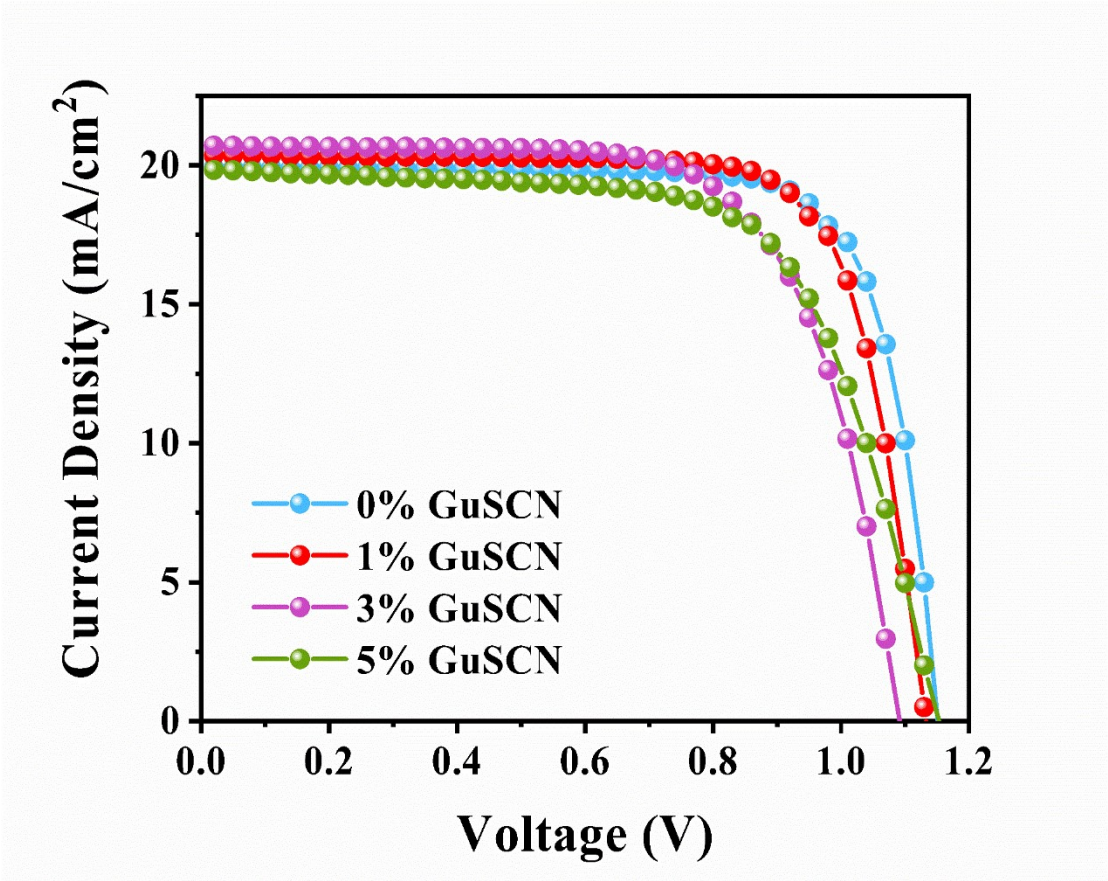

Fig. S10 The current-density-voltage curves of PSCs treated with GuSCN which was added into the perovskite precursor solution with a concentration of 1%-5%.

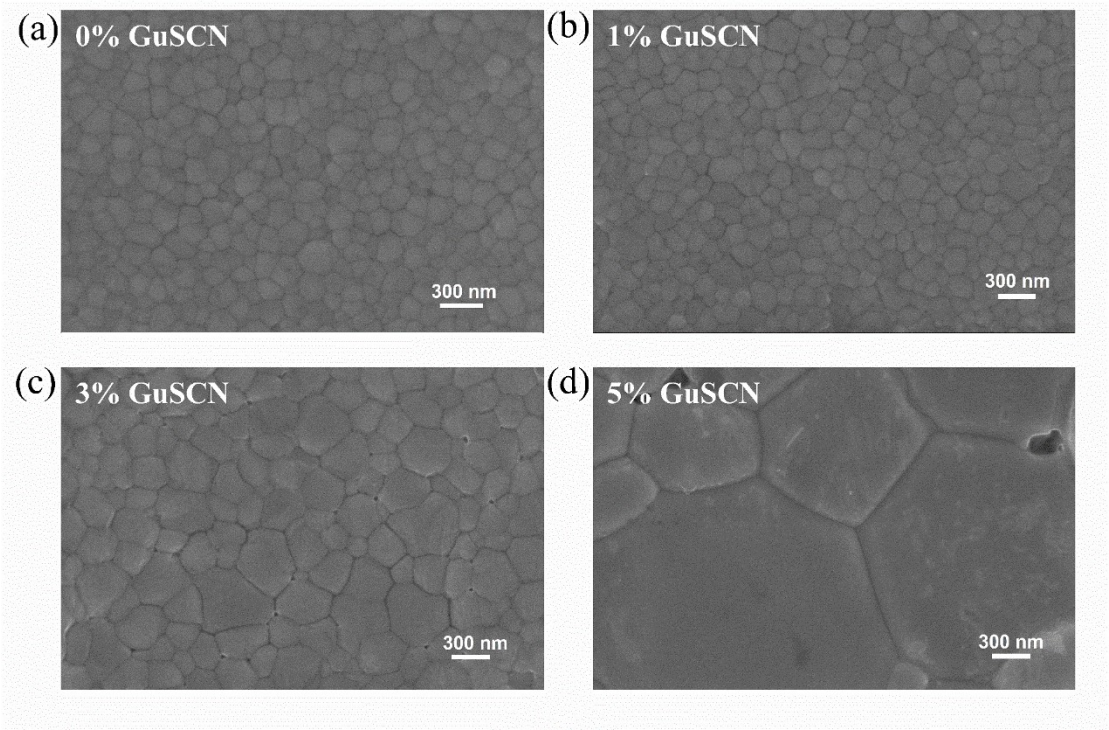

Fig. S11 SEM images of perovskite films treated with GuSCN which was added into the perovskite precursor solution with a concentration of 1%-5%.

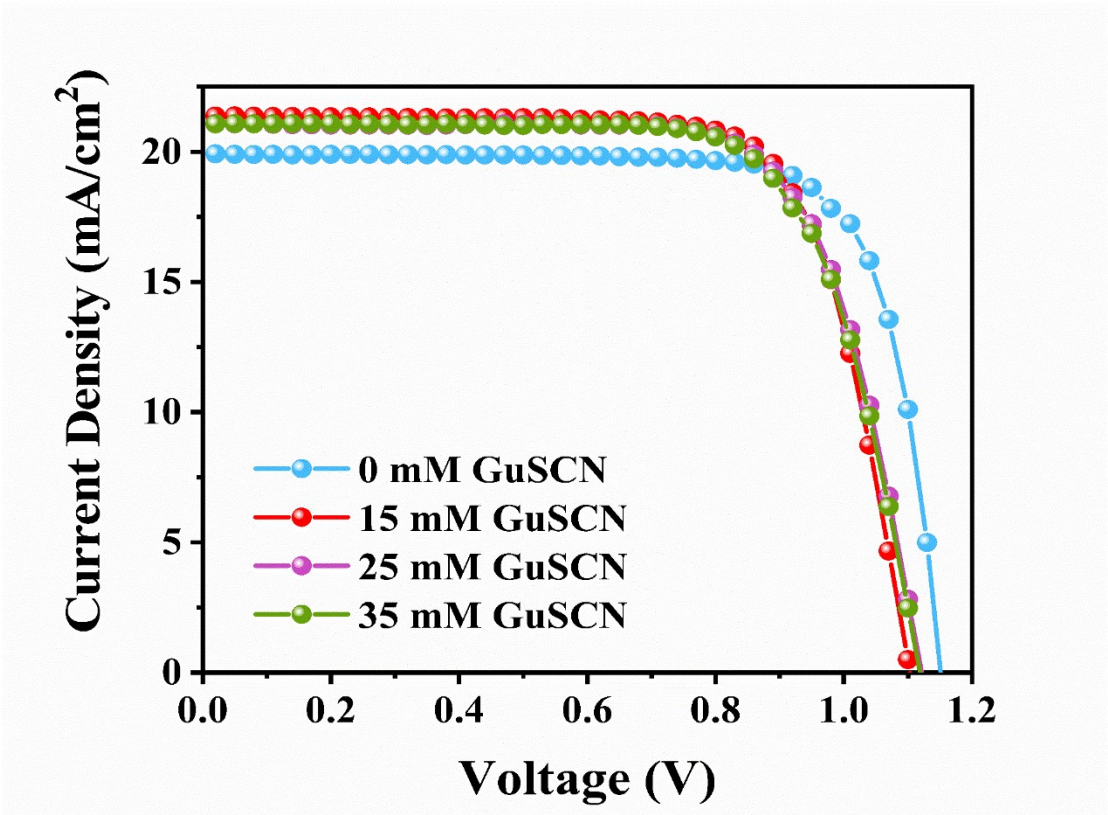

Fig. S12 The JV curves of PSCs with GuSCN modify the buried interface of perovskite.

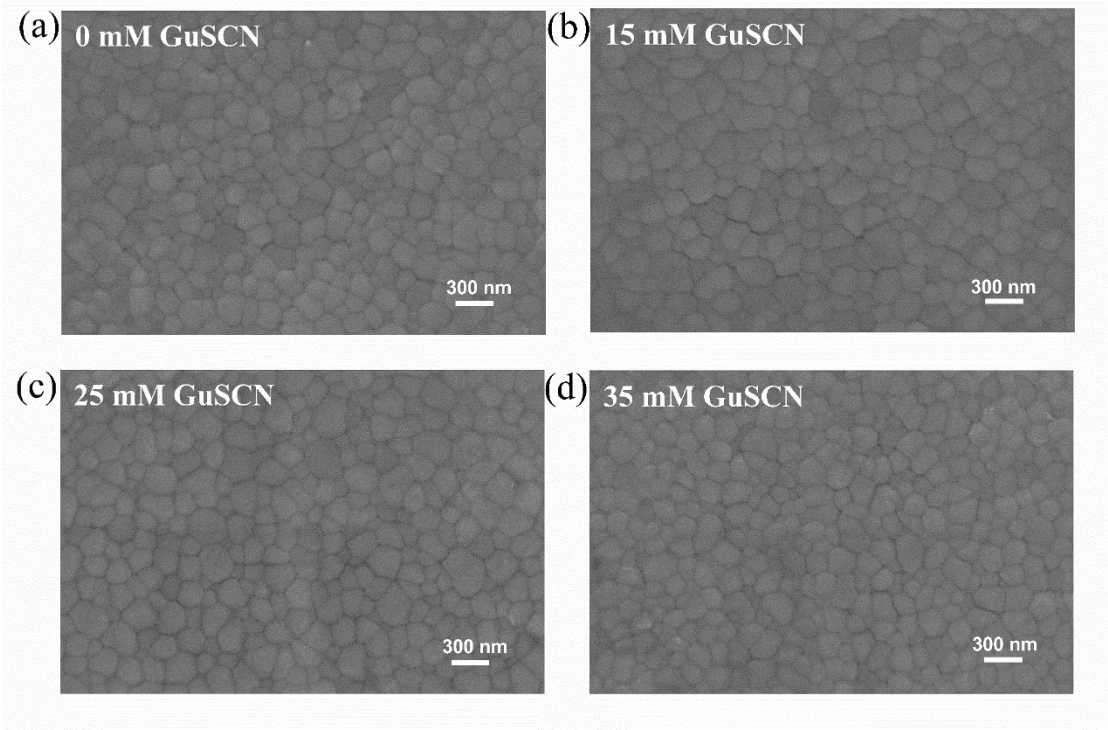

Fig. S13 SEM images of perovskite films on the NiO_x substrates modified with different concentrations of GuSCN.

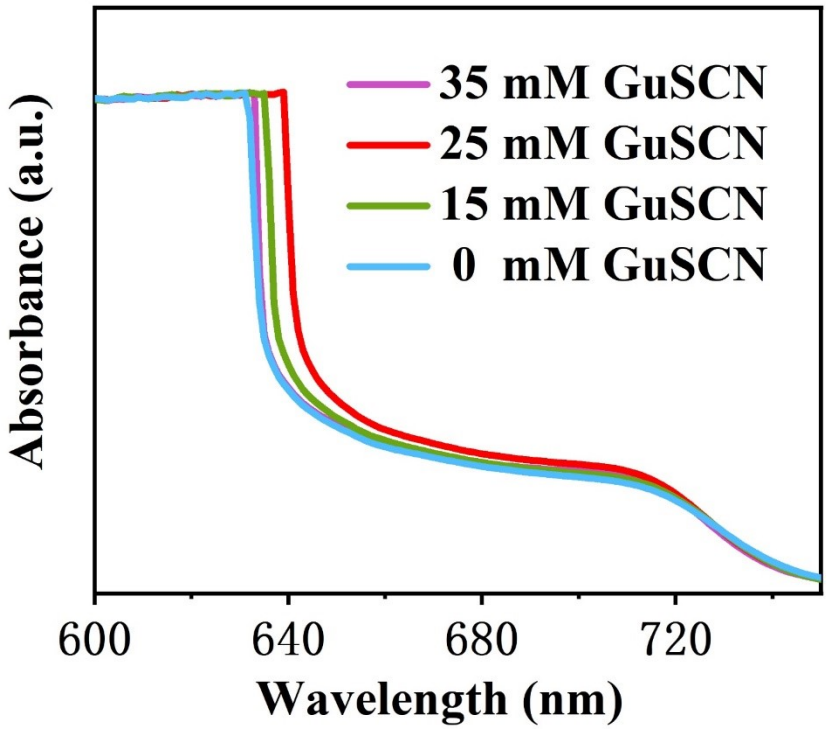

Fig. S14 UV–Vis absorption spectra of perovskite films post-treated with different concentrations of GuSCN.

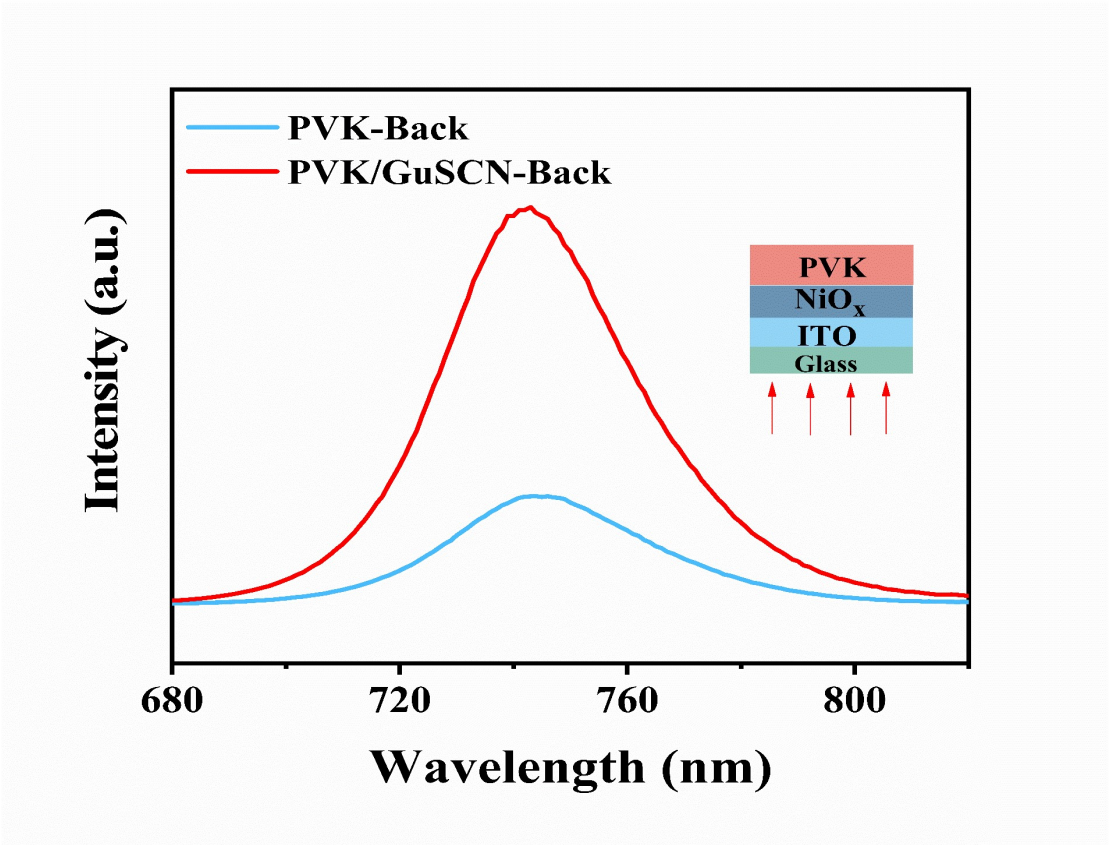

Fig. S15 Steady-state PL spectra of perovskite layer on glass with or without GuSCN with back incidence light.

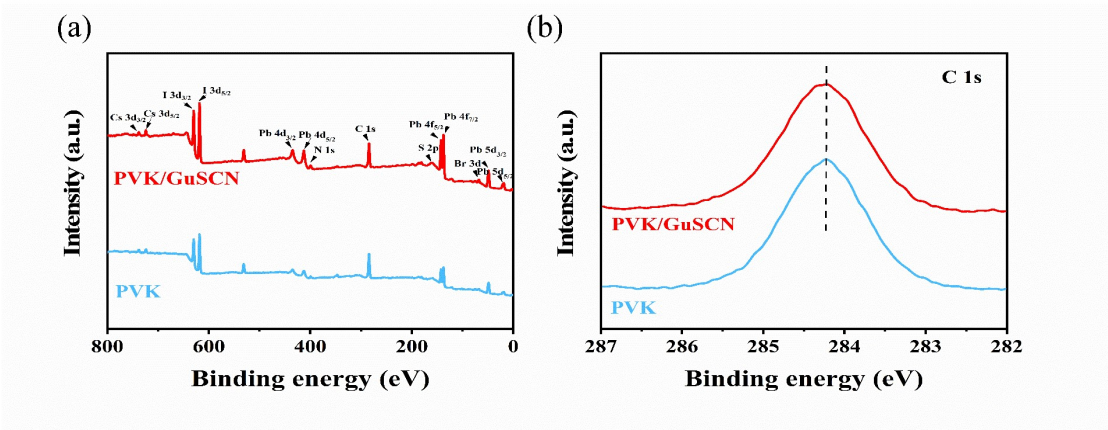

Fig. S16 (a) The complete XPS spectra and (b) XPS spectra of C 1s for control and GuSCN-treated perovskite films.

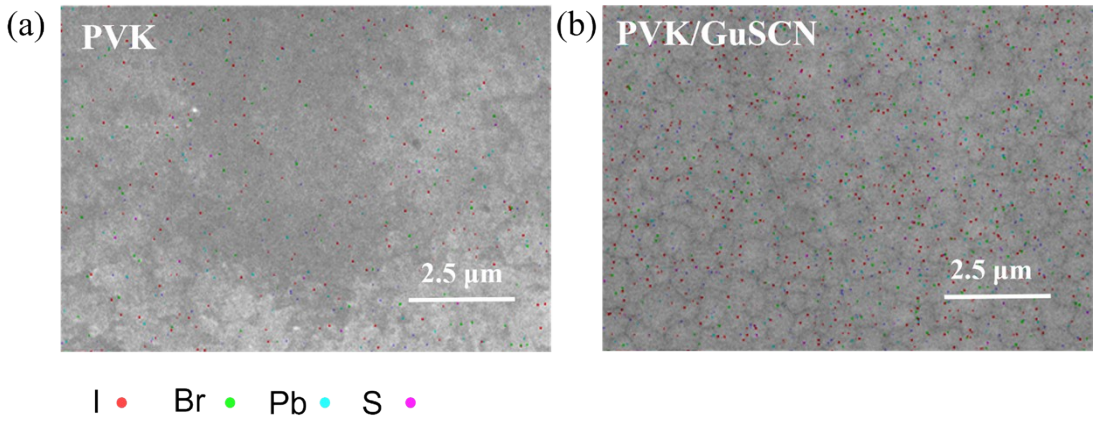

Fig. S17 EDS images of the control perovskite and perovskite treated with 25 mM GuSCN.

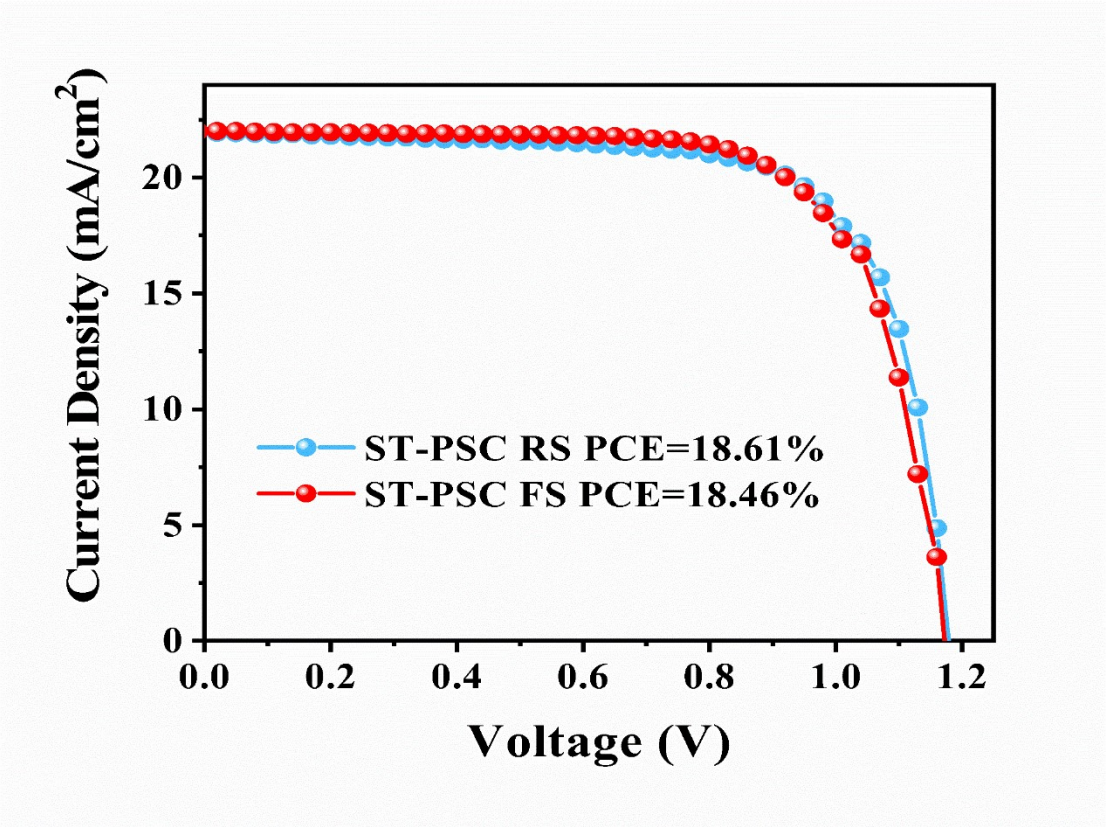

Fig. S18 The J-V curves of the semitransparent WBG-PSCs.

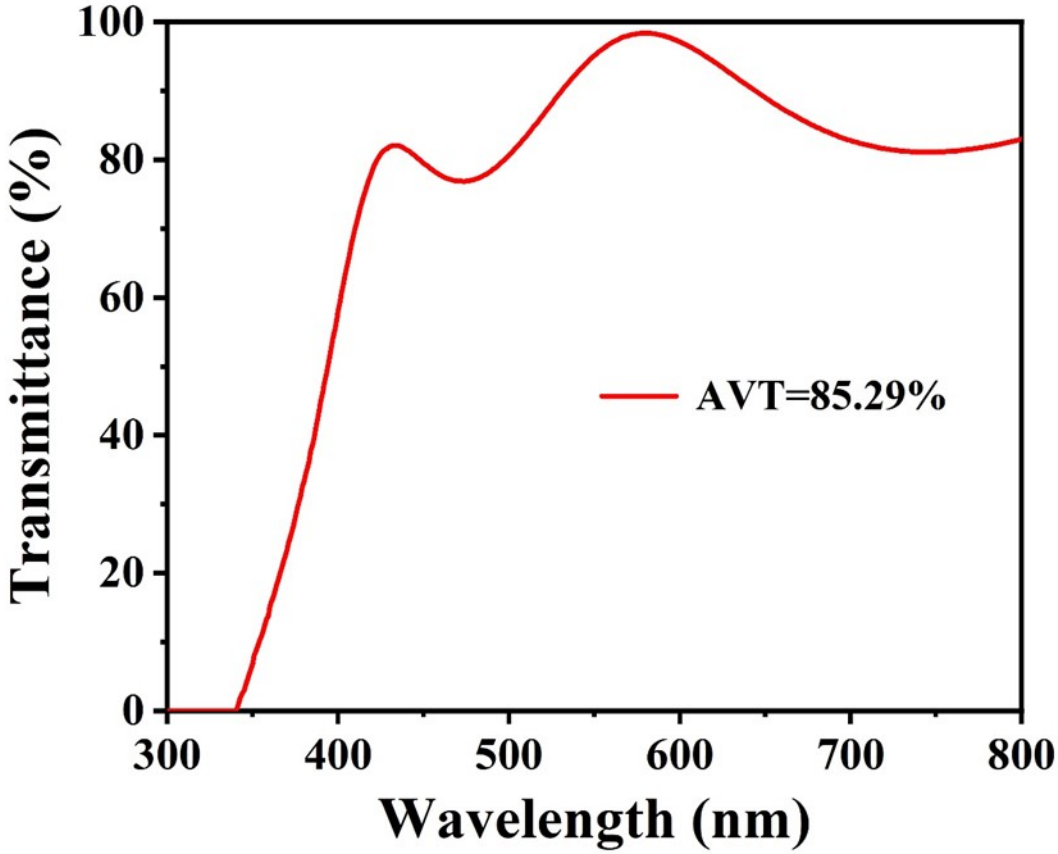

Fig. S19 Transmittance spectrum of ITO prepared in glass substrate by sputter.

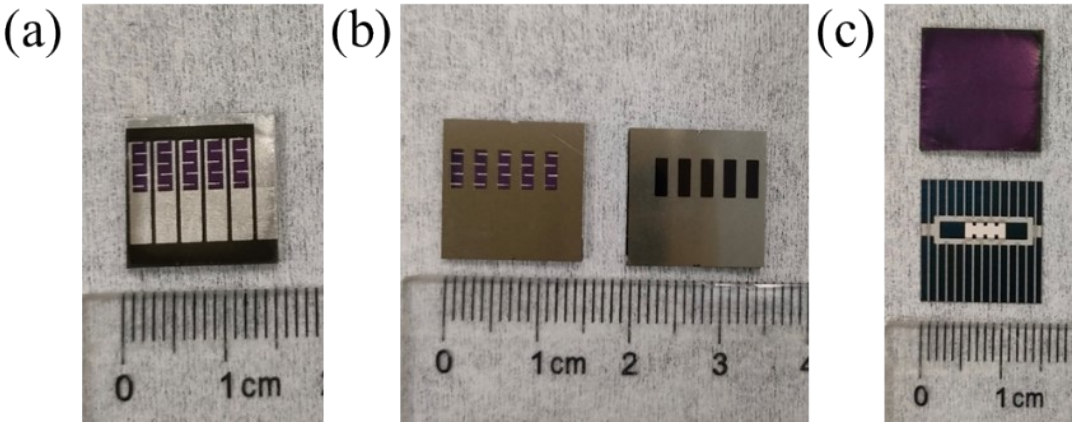

Fig. S20 The photos of (a) the semitransparent perovskite solar cells, (b) the semitransparent perovskite solar cells covered with a light mask, (c) the 2.25 cm^2 covered semitransparent perovskite solar cell and silicon-based solar cell.

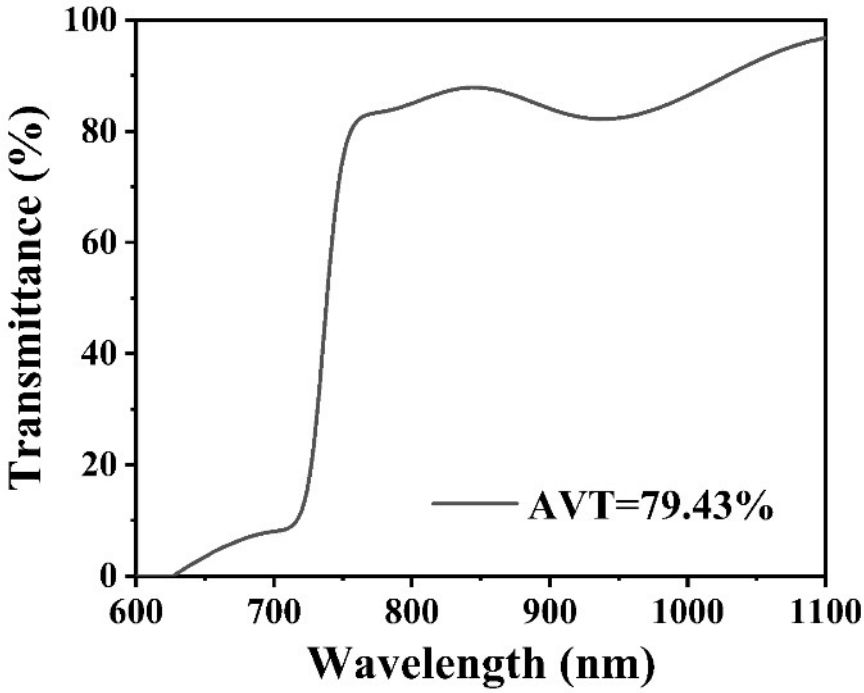

Fig. S21 Transmittance spectrum of the semi-transparent WBG PSC. The AVT is calculated from 700 nm to 1100 nm.

Table S1. Photoelectric performance parameters of PSCs in GuSCN with different concentrations.

	V_{OC} (V)	J_{SC} (mA/cm^2)	FF (%)	PCE (%)
0 mM GuSCN	1.15	19.92	77.22	17.67
15 mM GuSCN	1.18	20.59	79.81	19.46
25 mM GuSCN	1.20	21.26	82.04	20.92
35 mM GuSCN	1.21	21.16	66.27	16.93

Table S2. Photoelectric performance parameters of PSCs based on WBG perovskites.

	Perovskite	V_{OC} (V)	J_{SC} (mA/cm^2)	FF (%)	PCE (%)	Eg (eV)
[1]	$FA_{0.8}Cs_{0.2}Pb(I_{0.7}Br_{0.3})_3$	1.185	19.60	79.00	18.30	1.70
[2]	$Cs_{0.25}FA_{0.75}Pb(Br_{0.2}I_{0.8})_3$	1.100	19.40	81.00	17.40	1.68
[3]	$FA_{0.75}Cs_{0.25}Pb(I_{0.8}Br_{0.2})_3$	1.217	20.18	83.16	20.42	1.67
[4]	$FA_{0.87}Cs_{0.13}Pb(I_{0.87}Br_{0.13})_3$	1.250	22.27	80.00	22.30	1.62
[5]	$FA_{0.6}Cs_{0.4}Pb(I_{0.7}Br_{0.3})_3$	1.320	18.22	83.08	19.85	1.77
[6]	$Cs_{0.2}FA_{0.8}Pb(I_{0.7}Br_{0.3})_3$	1.300	18.90	77.80	19.07	1.75
[7]	$Cs_{0.22}FA_{0.78}Pb(I_{0.85}Br_{0.15})_3$	1.190	20.33	81.69	19.76	1.67
[8]	$FA_{0.8}Cs_{0.2}(I_{0.7}Br_{0.3})_3$	1.210	19.30	86.50	20.20	1.75
[9]	$Cs_{0.2}FA_{0.8}Pb(I_{0.6}Br_{0.4})_3$	1.250	18.79	83.70	19.37	1.77
[10]	$Cs_{0.3}FA_{0.7}PbI_{2.7}Br_{0.3}$	1.187	21.30	79.81	20.17	1.68
[11]	$FA_{0.8}Cs_{0.2}Pb(I_{0.6}Br_{0.4})_3$	1.310	17.94	82.31	19.33	1.77
[12]	$FA_{0.8}Cs_{0.2}Pb(I_{0.7}Br_{0.3})_3$	1.260	18.60	79.30	18.58	1.75
[13]	$FA_{0.8}Cs_{0.2}Pb(I_{0.6}Br_{0.4})_3$	1.220	15.70	83.50	16.00	1.80
[14]	$FA_{0.8}Cs_{0.2}PbI_{1.8}Br_{1.2}$	1.214	17.80	79.44	17.17	1.77
[15]	$FA_{0.8}Cs_{0.2}PbI_{1.8}Br_{1.2})$	1.175	17.98	78.44	16.57	1.77
[16]	$(CsI)_{0.08}(PbI_{1.4}Br_{0.6})$	1.220	22.67	80.35	22.28	1.67
	$(CsI_{0.125}Br_{0.875})_{0.08}(PbI_{1.2}Br_{0.8})_{0.92}$	1.190	20.28	84.75	20.45	1.77

[17]	$FA_{0.78}Cs_{0.22}Pb(I_{0.82}Br_{0.15}Cl_{0.03})_3$	1.190	21.60	78.00	20.60	1.67
[18]	$FA_{0.15}Cs_{0.85}Pb(I_{0.73}Br_{0.27})_3$	1.240	19.83	73.70	18.13	1.72
[19]	$FA_{0.8}Cs_{0.2}Pb(I_{0.7}Br_{0.3})_3$	1.204	19.84	78.00	18.51	1.74
[20]	$FA_{0.8}Cs_{0.2}Pb(I_{0.8}Br_{0.2})_3$	1.190	20.94	81.80	20.31	1.68
[21]	$FA_{0.8}Cs_{0.2}Pb(I_{0.7}Br_{0.3})_3$	1.250	18.53	79.00	18.27	1.75
[22]	$FA_{0.83}Cs_{0.17}Pb(I_{0.6}Br_{0.4})_3$	1.200	19.40	75.10	17.10	1.74
[23]	$Cs_{0.2}FA_{0.8}Pb(I_{0.75}Br_{0.25})_3$	1.170	20.40	77.30	18.50	1.67
[24]	$FA_{0.83}Cs_{0.17}Pb(I_{0.75}Br_{0.25})_3$	1.220	19.10	82.00	19.07	1.69
[25]	$FA_{0.8}Cs_{0.2}Pb(I_{0.7}Br_{0.3})_3$	1.240	17.92	81.90	18.19	1.75
[26]	$BA_{0.05}(FA_{0.83}Cs_{0.17})_{0.91}Pb(I_{0.8}Br_{0.2})_3$	1.140	22.70	80.00	20.60	1.61
[27]	$Cs_{0.17}FA_{0.83}PbI_{2.5}Br_{0.5}$	1.190	19.56	77.00	17.92	1.67
[28]	$Cs_{0.25}FA_{0.75}Pb(Br_{0.2}I_{0.8})_3$	1.162	19.62	80.80	18.42	1.68
[29]	$FA_{0.6}Cs_{0.4}Pb(I_{0.7}Br_{0.3})_3$	1.100	19.40	81.00	17.40	1.68

Reference

[1] J. Liang, C. Chen, X. Hu, Z. Chen, X. Zheng, J. Li, H. Wang, F. Ye, M. Xiao, Z. Lu, Y. Xu, S. Zhang, R. Yu, C. Tao, G. Fang, Suppressing the Phase Segregation with Potassium for Highly Efficient and Photostable Inverted Wide-Band Gap Halide Perovskite Solar Cells, ACS applied materials & interfaces, 12(43), 48458–48466. https://doi.org/10.1021/acsami.0c10310.

[2] K. A. Bush, K. Frohna, R. Prasanna, R. E. Beal, T. Leijtens, S. A. Swifter, M. D. McGehee, Compositional Engineering for Efficient Wide Band Gap Perovskites with Improved Stability to Photoinduced Phase Segregation, ACS energy letters, 3, 428-435. https://doi.org/ 10.1021/acsenergylett.7b01255.

[3] J. Xu, C. C. Boyd, Z. J. Yu, A. F. Palmstrom, D. J. Witter, B. W. Larson, R. M. France, J. Werner, S. P. Harvey, E. J. Wolf, W. Weigand, S. Manzoor, M. F. A. M. van Hest, J. J. Berry, J. M. Luther, Z. C. Holman, M. D. McGehee, Triple-halide wide-band gap perovskites with suppressed phase segregation for efficient tandems, Science, 367(6482), 1097–1104.

https://doi.org/10.1126/science.aaz5074.

[4] R. Su, Z. Xu, J. Wu, D. Luo, Q. Hu, W. Yang , X. Yang , R. Zhang, H. Yu, TP. Russell, Q. Gong, W. Zhang, R. Zhu, Dielectric screening in perovskite photovoltaics, Nat Commun. 2021, 12, 2479. https://doi.org/10.1038/s41467-021-22783-z.

[5] H. Liu, J. Dong, P. Wang, B. Shi, Y. Zhao, X. Zhang, Suppressing the Photoinduced Halide Segregation in Wide-Bandgap Perovskite Solar Cells by Strain Relaxation, Adv. Funct. Mater. 2023, 33, 2303673. https://doi.org/10.1002/adfm.202303673.

[6] Y. Yu, R. Liu, C. Liu, X.-L. Shi, H. Yu, Z.-G. Chen, Synergetic Regulation of Oriented Crystallization and Interfacial Passivation Enables 19.1% Efficient Wide-Bandgap Perovskite Solar Cells, Adv. Energy Mater. 2022, 12, 2201509. https://doi.org/10.1002/aenm.202201509.

[7] R. Li, B. Chen, N. Ren, P. Wang, B. Shi, Q. Xu, H. Zhao, W. Han, Z. Zhu, J. Liu, Q. Huang, D. Zhang, Y. Zhao, X. Zhang, CsPbCl3-Cluster-Widened Bandgap and Inhibited Phase Segregation in a Wide-Bandgap Perovskite and its Application to NiOx-Based Perovskite/Silicon Tandem Solar Cells, Adv. Mater. 2022, 34, 2201451. https://doi.org/10.1002/adma.202201451.

[8] M. A. Mahmud, J. Zheng, S. Tang, G. Wang, J. Bing, A. D. Bui, J. Qu, L. Yang, C. Liao, H. Chen, S. P. Bremner, H. T. Nguyen, J. Cairney, A. W. Y. Ho-Baillie, Cation-Diffusion-Based Simultaneous Bulk and Surface Passivations for High Bandgap Inverted Perovskite Solar Cell Producing Record Fill Factor and Efficiency, Adv. Energy Mater. 2022, 12, 2201672. https://doi.org/10.1002/aenm.202201672.

[9] X. Shen, B. M. Gallant, P. Holzhey, J. A. Smith, K. A. Elmestekawy, Z. Yuan, P. V. G. M. Rathnayake, S. Bernardi, A. Dasgupta, E. Kasparavicius, T. Malinauskas, P. Caprioglio, O. Shargaieva, Y.-H. Lin, M. M. McCarthy, E. Unger, V. Getautis, A. Widmer-Cooper, L. M. Herz, H. J. Snaith, Chloride-Based Additive Engineering for Efficient and Stable Wide-Bandgap Perovskite Solar Cells. Adv. Mater. 2023, 35, 2211742. https://doi.org/10.1002/adma.202211742.

[10] J. Cao, Z. Fang, S. Liu, Tailoring the Cs/Br Ratio for Efficient and Stable Wide-Bandgap Perovskite Solar Cells. Sol. RRL, 7: 2200955. https://doi.org/10.1002/solr.202200955.

[11] J. Zhu, Y. Luo, R. He, C. Chen, Y. Wang, Z. Yi, J. Thiesbrummel, C. Wang, F. Lang, H. Lai, Y. Xu, J. Wang, Z. Zhang, W. Liang, G. Cui, S. Ren, H. Huang, Y. Wang, F. Yao, Q. Lin, L. Wu, M. Stolterfoht, F. Fu, D. Zhao, A donor–acceptor-type hole-selective contact reducing non-radiative recombination losses in both subcells towards efficient all-perovskite tandems. Nat Energy 8, 714–724 (2023). https://doi.org/10.1038/s41560-023-01274-z.

[12] Y. Wang, Y. Zhao, T. Ma, Y. An, R. He, C. Chen, S. Ren, F. Fu, D. Zhao, A universal close-space annealing strategy towards high-quality perovskite absorbers enabling efficient all-perovskite tandem solar cells, Nat Energy 7, 744–753 (2022). https://doi.org/10.1038/s41560-022-01076-9.

[13] J. Zhou, H. Qiu, T. Wen, Z. He, C. Zou, Y. Shi, L. Zhu, C.-C. Chen, G. Liu, S. Yang, F.

Liu, Z. Yang, Acidity Control of Interface for Improving Stability of All-Perovskite Tandem Solar Cells, Adv. Energy Mater. 2023, 13, 2300968. https://doi.org/10.1002/aenm.202300968.

[14] H. Bi, J. Liu, Z. Zhang, L. Wang, D. Beresneviciute, R. Tavgeniene, G. Kapil, C. Ding, A.K. Baranwal, S.R. Sahamir, Y. Sanehira, H. Segawa, S. Grigalevicius, Q. Shen, S. Hayase, All-Perovskite Tandem Solar Cells Approach 26.5% Efficiency by Employing Wide Bandgap Lead Perovskite Solar Cells with New Monomolecular Hole Transport Layer. ACS Energy Letters. 2023, 8, 3852. https://doi.org/10.1021/acsenergylett.3c01275.

[15] H. Bi, Y. Fujiwara, G. Kapil, D. Tavgeniene, Z. Zhang, L. Wang, C. Ding, S. R. Sahamir, A. K. Baranwal, Y. Sanehira, K. Takeshi, G. Shi, T. Bessho, H. Segawa, S. Grigalevicius, Q. Shen, S. Hayase, Perovskite Solar Cells Consisting of PTAA Modified with Monomolecular Layer and Application to All-Perovskite Tandem Solar Cells with Efficiency over 25%, Adv. Funct. Mater. 2023, 33, 2300089. https://doi.org/10.1002/adfm.202300089.

[16] P. Hang, C. Kan, B. Li, Y. Yao, Z. Hu, Y. Zhang, J. Xie, Y. Wang, D. Yang, X. Yu, Highly Efficient and Stable Wide-Bandgap Perovskite Solar Cells via Strain Management, Adv. Funct. Mater. 2023, 33, 2214381. https://doi.org/10.1002/adfm.202214381.

[17] X. Liu, J. Zhang, L. Tang, J. Gong, W. Li, Z. Ma, Z. Tu, Y. Li, R. Li, X. Hu, Over 28% efficiency perovskite/Cu (InGa) Se 2 tandem solar cells: highly efficient sub-cells and their bandgap matching, Energy Environ. Sci. 2023, 16, 5029. https://doi.org/10.1039/D3EE00869J.

[18] Y. Zhou, F. Wang, Y. Cao, J.-P. Wang, H.-H. Fang, M. A. Loi, N. Zhao, C.-P. Wong, Benzylamine-treated wide-bandgap perovskite with high thermal‐photostability and photovoltaic performance, Adv. Energy Mater. 2017, 7, 1701048. https://doi.org/10.1002/aenm.201701048.

[19] T. Bu, J. Li, Q. Lin, D. P. McMeekin, J. Sun, M. Wang, W. Chen, X. Wen, W. Mao, C. R. McNeill, W. Huang, X. Zhang, J. Zhong, Y. Cheng, U. Bach, F. Huang, Structure engineering of hierarchical layered perovskite interface for efficient and stable wide bandgap photovoltaics, *Nano Energy, 75*, 104917. https://doi.org/10.1016/j.nanoen.2020.104917.

[20] C. Chen, J. Liang, J. Zhang, X. Liu, X. Yin, H. Cui, H. Wang, C. Wang, Z. Li, J. Gong, Q. Lin, W. Ke, C. Tao, B. Da, Z. Ding, X. Xiao, G. Fang, Interfacial engineering of a thiophene-based 2D/3D perovskite heterojunction for efficient and stable inverted wide-bandgap perovskite solar cells, Nano Energy. 2021, 90, 104917. https://doi.org/10.1016/j.nanoen.2021.106608.

[21] Y. Yu, C. Wang, C. R. Grice, N. Shrestha, D. Zhao, W. Liao, L. Guan, R. A. Awni, W. Meng, A. J. Cimaroli, K. Zhu, R. J. Ellingson, Y. Yan, Synergistic Effects of Lead Thiocyanate Additive and Solvent Annealing on the Performance of Wide-Bandgap Perovskite Solar Cells, ACS Energy Letters, 2017, 2 (5), 1177. https://doi.org/10.1021/acsenergylett.7b00278.

[22] D. P. McMeekin, G. Sadoughi, W. Rehman, G. E. Eperon, M. Saliba, M. T. Hörantner, A. A.Haghighirad, N. Sakai, L. Korte, B. Rech, M. B. Johnston, L. M. Herz, J. H. Snaith, A mixed-cation lead mixed-halide perovskite absorber for tandem solar cells, Science. 2016, 351,

151. https://doi.org/10.1126/science.aad5845.

[23] H. Tan, F. Che, M. Wei, Y. Zhao, M. I. Saidaminov, P. odorović, D. Broberg, G. Walters, F. Tan, T. Zhuang, B. Sun, Z. Liang, H. Yuan, E. Fron, J. Kim, Z. Yang, O. Voznyy, M. Asta, E. H. Sargent, Dipolar cations confer defect tolerance in wide-bandgap metal halide perovskites, Nat Commun. 2018, 9, 3100. https://doi.org/10.1038/s41467-018-05531-8.

[24] M. Taddei, J. A. Smith, B. M. Gallant, S. Zhou, R. J. E. Westbrook, Y. Shi, J. Wang, J. N. Drysdale, D. P. McCarthy, S. Barlow, S. R. Marder, H. J. Snaith, D. S. Ginger, Ethylenediamine Addition Improves Performance and Suppresses Phase Instabilities in Mixed-Halide Perovskites, ACS Energy Letters. 2022, 7 (12), 4265-4273. https://doi.org/10.1021/acsenergylett.2c01998.

[25] C. Chen, Z. Song, C. Xiao, D. Zhao, N. Shrestha, C. Li, G. Yang, F. Yao, X. Zheng, R. J. Ellingson, C. Jiang, M. Al-Jassim, K. Zhu, G. Fang, Y. Yan, Achieving a high open-circuit voltage in inverted wide-bandgap perovskite solar cells with a graded perovskite homojunction, Nano Energy. 2019, 61, 141. https://doi.org/10.1016/j.nanoen.2019.04.069.

[26] Z. Wang, Q. Lin, F. P. Chmiel, N. Sakai, L. M. Herz, H. J. Snaith, Efficient ambient-air-stable solar cells with 2D–3D heterostructured butylammonium-caesium-formamidinium lead halide perovskites, Nat Energy 2, 17135 (2017). https://doi.org/10.1038/nenergy.2017.135.

[27] M. Z. Long, T. K. Zhang, M. Z. Liu, Z. F. Chen, C. Wang, W. G. Xie, F. Y. Xie, J. Chen, G. Li, J. B. Xu, Abnormal Synergetic Effect of Organic and Halide Ions on the Stability and Optoelectronic Properties of a Mixed Perovskite via In Situ Characterizations, Adv. Mater. 2018, 30, 1801562. https://doi.org/10.1002/adma.201801562.

[28] J. A. Raiford, C. C. Boyd, A. F. Palmstrom, E. J. Wolf, B. A. Fearon, J. J. Berry, M. D. McGehee, S. F. Bent, Enhanced Nucleation of Atomic Layer Deposited Contacts Improves Operational Stability of Perovskite Solar Cells in Air. Adv. Energy Mater. 2019, 9, 1902353. https://doi.org/10.1002/aenm.201902353.

[29] K. A. Bush, K. Frohna, R. Prasanna, R. E. Beal, T. Leijtens, S. A. Swifter, M. D. McGehee, Compositional Engineering for Efficient Wide Band Gap Perovskites with Improved Stability to Photoinduced Phase Segregation, ACS Energy Letters. 2018, 3 (2), 428. https://doi.org/10.1021/acsenergylett.7b01255

Table S3. The average data of 30 PSCs were summarized.

	V_{OC} (V)	J_{SC} (mA/cm^2)	FF (%)	PCE (%)
Target	1.212±0.01	20.62±1.08	78.90±1.67	19.70±0.87
Control	1.146±0.02	20.20±0.31	75.30±1.85	17.43±0.53

Table S4. Photovoltaic performance parameters of PSCs treated with GuSCN. The GuSCN with concentrations varying from 1% to 5% was added to the perovskite precursor solution.

	V_{OC} (V)	J_{SC} (mA/cm^2)	FF (%)	PCE (%)
0% GuSCN	1.15	19.92	77.22	17.67
1% GuSCN	1.13	20.35	75.80	17.45
3% GuSCN	1.09	20.70	68.59	15.50
5% GuSCN	1.15	19.87	67.01	15.34

Table S5. Photoelectric performance parameters of PSCs with GuSCN modifying the buried interface of perovskite.

	V_{OC} (V)	J_{SC} (mA/cm^2)	FF (%)	PCE (%)
0 mM GuSCN	1.15	19.92	77.22	17.67
15 mM GuSCN	1.10	21.38	73.96	17.44
25 mM GuSCN	1.12	21.08	72.45	17.12
35 mM GuSCN	1.12	21.09	71.80	16.93

Table S6. Fitted lifetime results of perovskite and passivated perovskite with GuSCN, where τ_1 and τ_2 refer to fast and slow decay lifetimes respectively, and $\tau_{average}$ is intensity weighted.

Treatment	A_1	τ_1(ns)	A_2	τ_2(ns)	$\tau_{average}$(ns)
Perovskite	0.12	18	0.66	535	532
Perovskite/GuSCN	0.78	430	0.27	3150	2380

Table S7. Atomic ratio of the elements derived from EDS.

	I（%）	Br（%）	Pb (%)	S (%)	I/Br
Control	58.17	17.27	24.55	0	3.37
Target	59.36	15.17	24.87	0.60	3.92

Table S8. Photovoltaic parameters of the semitransparent WBG-PSCs.

	V_{OC} (V)	J_{SC} (mA/cm^2)	FF (%)	PCE (%)
ST-PSC RS	1.18	21.90	72.25	18.61
ST-PSC FS	1.17	22.01	71.53	18.46

Table S9. 4-T tandem solar cell.

	V_{OC} (V)	J_{SC} (mA/cm^2)	FF (%)	PCE (%)
PVK	1.18	21.90	72.25	18.61
Original Si	0.69	40.84	73.75	20.60
Filtered Si	0.66	17.30	75.25	8.55
4-T tandem	/	/	/	27.16